International Journal of Hydrogen Energy 248 (2026) 155902

Contents lists available at ScienceDirect

International Journal of Hydrogen Energy

journal homepage: www.elsevier.com/locate/he

Interfacial engineering of $ZnIn_2S_4/Ti_3CN$ MXene heterojunctions enables efficient photocatalytic hydrogen evolution via band alignment and rapid charge separation

Yakun Song, Huajun Gu, Yifan Liao, Jiayi Meng, Yamei Huang, Quanmei Zhou, Yuchen Wei, Yuying Hu, Mohan Zhang, Bite Deng, Wei-Lin Dai *

State Key Laboratory of Porous Materials for Separation and Conversion, Shanghai Key Laboratory of Molecular Catalysis and Innovative Materials, Department of Chemistry, Fudan University, Shanghai, 200438, PR China

ARTICLE INFO

Keywords:
$Ti_3CN/ZnIn_2S_4$ heterojunction
Non-Ti_3C_2-type MXene
Built-in electric field
Gibbs free energy of hydrogen adsorption
Photocatalytic hydrogen evolution

ABSTRACT

Overcoming rapid charge carrier recombination and restricted visible-light harvesting in single-component photocatalysts remains a formidable challenge for efficient solar-to-hydrogen conversion. In this work, an in situ self-assembly strategy is employed to construct a high-performance heterojunction by integrating zinc indium sulfide ($ZnIn_2S_4$) nanoflowers with non-Ti_3C_2-type titanium carbonitride (Ti_3CN) MXene nanosheets. The optimized 3 wt% $Ti_3CN/ZnIn_2S_4$ composite exhibits a remarkable visible-light-driven hydrogen evolution rate of 603.3 μmol g^{-1} h^{-1}, which represents a 2.4-fold enhancement over pristine $ZnIn_2S_4$ while maintaining exceptional cyclic stability. Ultra-violet photoelectron spectroscopy analysis and Density functional theory calculations reveal that the higher work function of Ti_3CN (4.58 eV) compared to $ZnIn_2S_4$ (4.07 eV) drives upward band bending at the interface, thereby establishing a robust built-in electric field. This tailored architecture facilitates ultrafast, directional electron injection from $ZnIn_2S_4$ to the Ti_3CN matrix, effectively suppressing charge recombination. Furthermore, the Ti_3CN component serves as a superior electron sink where the calculated Gibbs free energy of hydrogen adsorption (ΔG_{H^*}) is optimized to −0.21 eV, leading to a significantly reduced reaction overpotential. This study provides a robust strategy for the rational design of MXene-based heterojunctions and offers a solid foundation for green hydrogen production in large-scale renewable systems.

1. Introduction

The increasing demand for clean energy and carbon-neutral technologies has stimulated intensive research on solar-to-chemical energy conversion [1–5]. Among various renewable-energy routes, photocatalytic water splitting provides a promising strategy for directly converting solar energy into storable hydrogen fuel [6,7]. Hydrogen is regarded as an attractive secondary energy carrier because of its high gravimetric energy density and clean utilization process [8,9]. Nevertheless, practical solar hydrogen production still relies heavily on the development of photocatalysts with efficient light harvesting, rapid charge separation, abundant reaction sites, and long-term stability [10].

Extensive efforts have been devoted to photocatalytic platforms such as metal oxides [11,12], graphitic carbon nitride (g-C_3N_4) [13,14], metal sulfides [15,16], and metal-organic frameworks (MOFs) [17,18]. Among them, zinc indium sulfide ($ZnIn_2S_4$), a representative ternary metal chalcogenide, has attracted considerable attention for photocatalytic hydrogen evolution owing to its visible-light response, suitable band structure, low toxicity, and good physicochemical stability [19–21]. However, pristine $ZnIn_2S_4$ still suffers from rapid recombination of photogenerated electron–hole pairs and insufficient surface catalytic kinetics. Recent studies have shown that defect/doping regulation and lattice-strain engineering can effectively improve charge separation and surface proton-reduction kinetics in $ZnIn_2S_4$-based systems [22,23]. Meanwhile, alloy cocatalyst modification and S-scheme heterojunction construction have been demonstrated as efficient approaches to promote carrier migration while maintaining strong redox capability [24,25]. More recently, plasmonic coupling, dual built-in electric fields, and MOF-derived core-shell interfaces have further expanded the structural design strategies for $ZnIn_2S_4$-based photocatalytic H_2 evolution [26–28]. Recent reviews have also summarized the rapid development of $ZnIn_2S_4$-based hybrid materials and composite photocatalysts for

* Corresponding author.
E-mail address: wldai@fudan.edu.cn (W.-L. Dai).

https://doi.org/10.1016/j.ijhydene.2026.155902
Received 17 March 2026; Received in revised form 1 May 2026; Accepted 3 June 2026
Available online 8 June 2026

hydrogen evolution and solar-to-chemical conversion [29–31].

To overcome the intrinsic kinetic limitations of semiconductor photocatalysts, rational heterostructure construction has been widely adopted to broaden light absorption and accelerate spatial charge separation. In this context, $ZnIn_2S_4$/MXene-related systems have recently demonstrated that MXenes can act as charge-transport layers or electronic bridges to facilitate interfacial carrier migration [32,33]. More broadly, two-dimensional materials are attractive for interfacial charge regulation because their short carrier-transport pathways and abundant surface sites are favorable for electron migration [34,35]. MXenes, as a rapidly developing family of two-dimensional transition-metal carbides, nitrides, and carbonitrides, possess metallic conductivity, tunable surface terminations, and rich surface metal sites, making them promising cocatalysts and electron mediators in photocatalytic systems [36,37]. Nevertheless, most MXene-assisted photocatalytic systems still focus on conventional MXene compositions, especially Ti_3C_2-based structures, whereas the role of non- Ti_3C_2-type titanium carbonitride MXenes in regulating $ZnIn_2S_4$ band alignment and charge-transfer behavior remains insufficiently explored [38,39].

Herein, we construct a close-contact $ZnIn_2S_4$/Ti_3CN heterojunction through an in situ self-assembly strategy. By introducing Ti_3CN as a non-Ti_3C_2-type MXene component, this work aims to establish an efficient interfacial electron-transfer pathway, suppress charge recombination, and clarify the role of Ti_3CN in band regulation and photocatalytic H_2 evolution. This study provides a non-Ti_3C_2-type MXene-assisted strategy for designing $ZnIn_2S_4$-based heterojunction photocatalysts with improved charge separation and surface reaction kinetics.

2. Experimental

2.1. Preparation of Ti_3CN MXene nanosheets

Ti_3CN MXene nanosheets were synthesized via a modified oxidative etching process using a LiF–HCl solution. Typically, 2 g of Ti_3AlCN precursor powder was gradually introduced into an etchant mixture consisting of 3.2 g of LiF dissolved in 40 mL of 9 M HCl. The suspension was maintained at 40 °C under continuous stirring for 24 h to facilitate the selective removal of Al layers. Following the etching process, the resulting solid residue was harvested and subjected to several washing cycles with 1 M HCl and deionized water (DI) through repeated centrifugation until the supernatant reached a neutral pH (≈6–7). To achieve effective exfoliation, the sediment was re-dispersed in DI water and subjected to multiple oscillation-centrifugation cycles, followed by probe sonication for 1 h. Finally, the colloidal dispersion was centrifuged at 3500 rpm for 30 min, with the dark-colored supernatant being collected to obtain the delaminated Ti_3CN MXene nanosheets.

2.2. Preparation of $ZnIn_2S_4$ nanoflowers

$ZnIn_2S_4$ nanoflowers were synthesized by a simple hydrothermal method. Firstly, 1.8 mmol (244.8 mg) of $ZnCl_2$ and 1.8 mmol (527.7 mg) of $InCl_3{\cdot}4H_2O$ were dissolved in 24 mL of H_2O and stirred for 15 min. Then, 3.6 mmol of thioacetamide and 6 mL of glycerol were added to the solution. The mixture was transferred to a water bath at 80 °C and stirred continuously for 2 h. After cooling, the product was washed with 0.1 M dilute hydrochloric acid, followed by repeated washing with water and ethanol. Finally, $ZnIn_2S_4$ nanoflower catalysts were obtained after freeze-drying.

2.3. Preparation of $ZnIn_2S_4$–Ti_3CN composites

$ZnIn_2S_4$–Ti_3CN composites were synthesized via electrostatic self-assembly. Firstly, $ZnIn_2S_4$ nanoflowers were prepared according to the synthesis procedure described in the above. Then, 100 mg of $ZnIn_2S_4$ powder was dispersed in 100 mL of water and fully ultrasonicated to form a homogeneous solution. A certain amount of freshly prepared Ti_3CN MXene nanosheet solution (concentration: 10 mg/mL) was added to the $ZnIn_2S_4$ solution, and the mixture was magnetically stirred under an inert atmosphere for 1 h. The resulting suspension was freeze-dried until completely dry to obtain $ZnIn_2S_4$–Ti_3CN composite powder. In addition, to investigate the effect of different mass ratios on photocatalytic performance, $ZnIn_2S_4$–Ti_3CN composites with different Ti_3CN MXene mass fractions (1%, 3%, 5%, 7%) were prepared by adjusting the addition amount of Ti_3CN MXene solution. In the subsequent experiments of this work, "$ZnIn_2S_4$–Ti_3CN" specifically refers to the sample with a Ti_3CN MXene mass fraction of 3% relative to $ZnIn_2S_4$. For comparison, 1%Pt–$ZnIn_2S_4$ (1% Pt mass fraction relative to $ZnIn_2S_4$) was prepared by the photodeposition method.

2.4. Characterization and theoretical method

The apparatus for the characterization and the computational details can be found in the Supporting ***Information***.

3. Results and discussion

3.1. Materials synthesis and characterization

The preparation process of the $ZnIn_2S_4$– Ti_3CN composite catalyst is illustrated in Fig. 1 (a). The specific steps are as follows: HF generated in situ by the reaction of LiF and HCl was used to etch the Al layer in the Ti_3AlCN MAX phase, thereby preparing multilayer Ti_3CN MXene. These multilayer Ti_3CN MXene were further treated with ultrasonic exfoliation technology to obtain single-layer Ti_3CN nanosheets. Through this electrostatic self-assembly approach, the pre-synthesized $ZnIn_2S_4$ nanoflowers were effectively integrated with the exfoliated Ti_3CN nanosheets. This strategy successfully constructs an intimately coupled heterostructure, ensuring a seamless interface that is essential for facilitating efficient charge communication between the two components.

The morphological features and structural evolution of the as-prepared samples were systematically investigated through a combination of scanning electron microscopy (SEM), atomic force microscopy (AFM), and transmission electron microscopy (TEM). It can be seen from the TEM and SEM image that $ZnIn_2S_4$ exhibits a nanoflower morphology. As shown in the TEM image (Fig. 1 (b)) and the SEM image (Fig. 1 (c)), $ZnIn_2S_4$ exhibits a typical nanoflower-like morphology. SEM characterization results (Fig. 1 (d) and 1 (e)) show that the pristine Ti_3AlCN MAX phase exhibits a bulk structure. After the etching and exfoliation process, this structure transforms into Ti_3CN nanosheets, which on a porous anodic aluminum oxide substrate, intuitively demonstrating the morphological evolution from the bulk Ti_3AlCN MAX phase to Ti_3CN nanosheets. Fig. 1(f–j) and Fig. S1 present the TEM and AFM characterizations of Ti_3CN nanosheets. The TEM image in Fig. 1 (f) reveals a layered nanosheet structure of Ti_3CN deposited on a copper grid. The high-angle annular dark-field scanning transmission electron microscopy (HAADF-STEM) image and the corresponding elemental mapping results (Fig. 1(g–j)) confirm the uniform distribution of Ti, C, N, and O elements within the Ti_3CN framework, demonstrating the successful synthesis of Ti_3CN nanosheets. AFM analysis further verifies the monolayer nature of Ti_3CN MXene. The height profile along the white line in Fig. 1 (k) and Fig. 1 (l) indicates a thickness of approximately 1.83 nm. Consistently, the three-dimensional AFM image in Fig. 1 (m) shows a nanosheet morphology with a thickness of about 1.80 nm, further confirming the single-layer structural characteristic of Ti_3CN MXene [40].

The morphology of the $ZnIn_2S_4$–Ti_3CN composite was characterized by TEM and SEM. TEM images (Fig. 2 (a)) show $ZnIn_2S_4$ nanoflowers anchored on Ti_3CN MXene nanosheets. In the HRTEM image (Fig. 2 (b–d)), lattice spacings of 0.32 nm and 0.27 nm are assigned to the (102) plane of $ZnIn_2S_4$ [41, 42] and the (100) plane of Ti_3CN MXene, respectively. A distinct interface is observed between the two

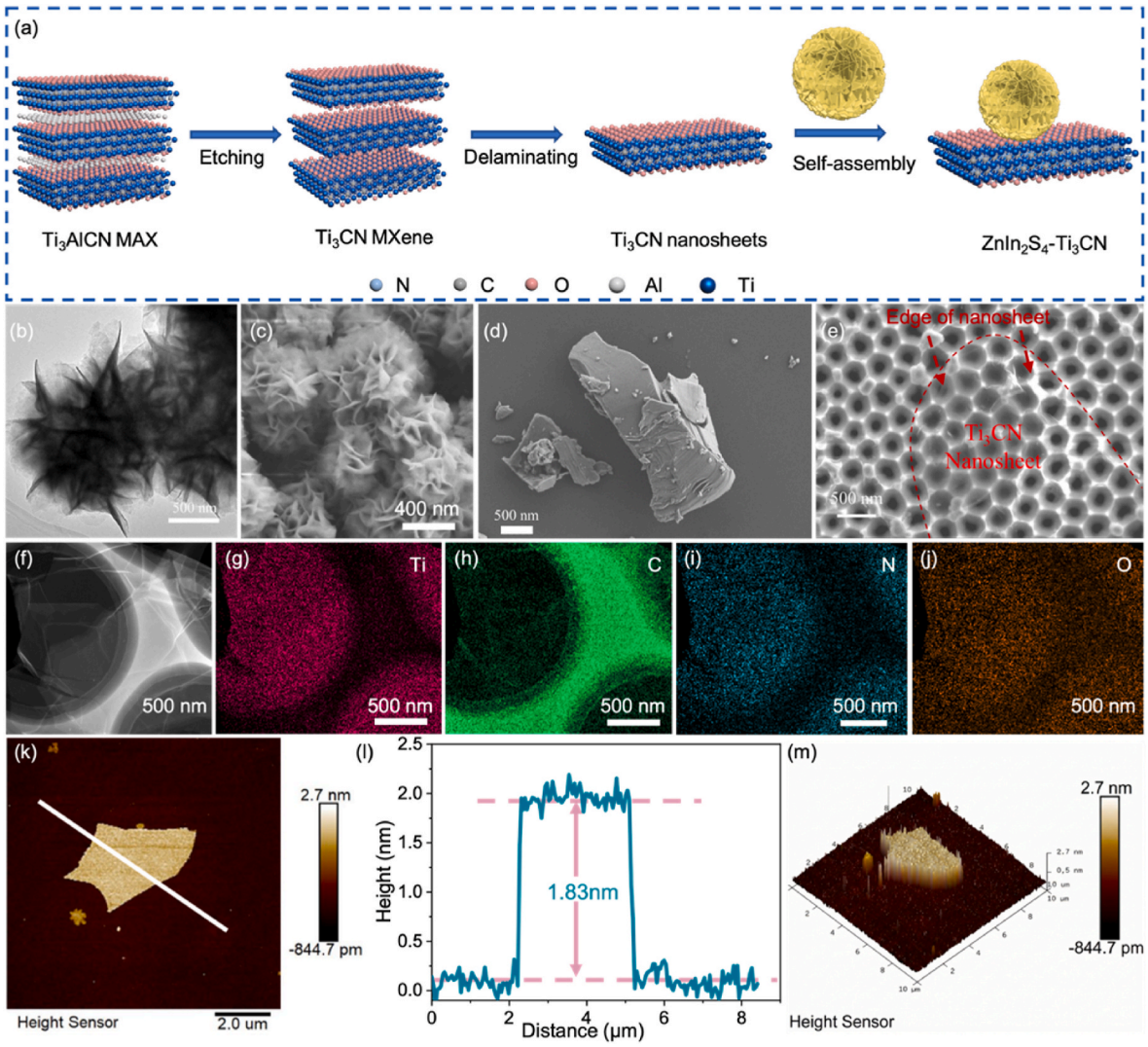

Fig. 1. (a) Schematic representation of the synthesis of $ZnIn_2S_4$–Ti_3CN MXene; (b) TEM image of $ZnIn_2S_4$; (c) SEM of pure $ZnIn_2S_4$; (d,e) SEM images of Ti_3AlCN and Ti_3CN; (f-j) HAADF-STEM images with corresponding EDS mappings for Ti, C, N, and O; (k, l) AFM image and height profile; (m) 3D AFM visualization.

components, indicating tight interfacial contact and heterojunction formation [43]. HAADF-STEM elemental mappings (Fig. 2(e–l)) show homogeneous distributions of the constituent elements, supporting the successful fabrication of the composite. SEM image (Fig. 2 (m)) further reveals Ti_3CN nanosheets covering the $ZnIn_2S_4$ nanoflowers, and the corresponding EDS mapings (Fig. 2(n–t)) confirm uniform elemental distribution. The ultrathin Ti_3CN MXene nanosheets enhance light absorption and facilitate electron transport owing to their high conductivity [44]. Meanwhile, few-layer Ti_3CN remains light-permeable, providing a structural basis for improved photocatalytic H_2 evolution. The slight mismatch between the C and Ti elemental maps is mainly attributed to the contribution of the carbon support film in TEM, since the C signal is not exclusively derived from Ti_3CN. Therefore, the Ti and N distributions provide more direct evidence for the spatial distribution of the Ti_3CN component.

The crystal structures of all samples were analyzed by X-ray diffraction (XRD). From the XRD pattern of Ti_3CN (Fig. 3 (a)), it can be seen that the main peak of the (104) crystal plane of Ti_3AlCN disappears, indicating that Al has been removed from Ti_3AlCN to form Ti_3CN MXene [43]. In addition, the (002) diffraction peak shifts to a lower angle relative to Ti_3AlCN, shifting negatively from 9.6° to 6.3°, which can be attributed to the increase in the interlayer spacing of Ti_3CN MXene, further proving the successful preparation of Ti_3CN MXene [44]. Fig. 3 (b) shows that the diffraction peaks at 21.6°, 27.5°, 47.3°, 52.5°, and 55.7° match the (006), (102), (112), (1012), and (022) crystal planes of $ZnIn_2S_4$ [45,46]. Fig. 3(c–d) are local magnification views of Fig. 3 (b). In Fig. 3(c–d), we observed that with the increase of Ti_3CN MXene content, the peak positions shift to higher angles, moving from 27.5° and 47.3° to 27.8° and 47.6° respectively. The observed lattice distortion strongly suggests a robust interfacial interaction between $ZnIn_2S_4$ and Ti_3CN MXene, further validating the successful construction of the $ZnIn_2S_4$–Ti_3CN heterojunction. To fully elucidate the underlying interaction mechanisms at the atomic level, comprehensive investigations and advanced spectroscopic analyses remain ongoing.

X-ray photoelectron spectroscopy (XPS) was employed to elucidate the surface composition and interfacial electronic interaction in the $ZnIn_2S_4$–Ti_3CN composite. The survey spectrum (Fig. 3 (e)) displays characteristic signals of Zn, In, and S from $ZnIn_2S_4$ together with Ti, C, and N from Ti_3CN MXene, confirming the coexistence of both components and consistent with the elemental distributions observed by TEM and SEM.

To elucidate the interfacial electronic modulations and directional charge migration, comprehensive XPS and in-situ light-irradiated XPS analyses were performed. In-situ light-irradiated XPS has recently been demonstrated as an effective technique for tracking photoinduced charge redistribution and electron-transfer pathways in heterojunction

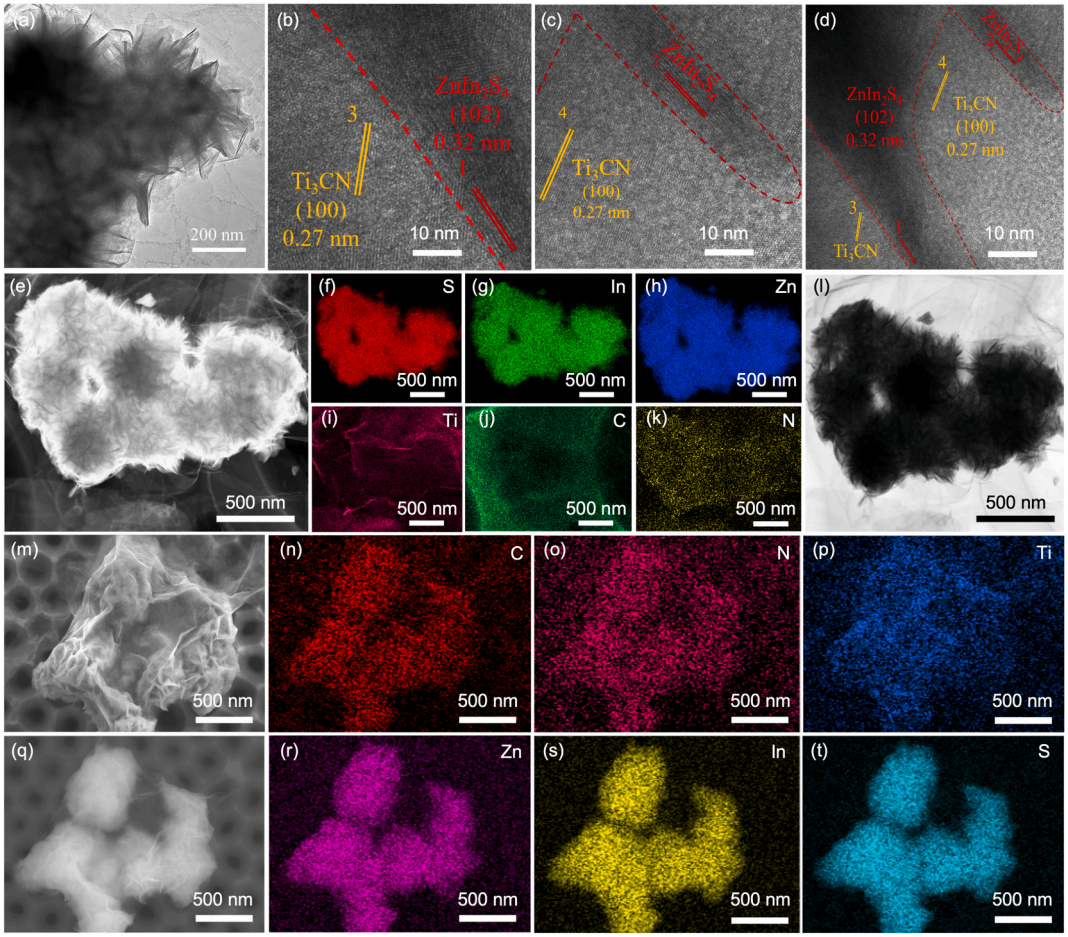

Fig. 2. (a-d) TEM and HRTEM of $ZnIn_2S_4$–Ti_3CN composite; (e-k) HAADF-STEM images of the $ZnIn_2S_4$–Ti_3CN composite with corresponding EDS mappings for S, In, Zn, Ti, C, N elements; (e-k) SEM of pure $ZnIn_2S_4$; (l) Bright field TEM image of $ZnIn_2S_4$–Ti_3CN composite; (m-t) SEM of $ZnIn_2S_4$–Ti_3CN composite with corresponding EDS mappings for elements S, In, Zn, Ti, C, N.

photocatalysts, since light-triggered binding-energy shifts can reflect changes in the local electron density of specific elements [47–51]. Therefore, the binding-energy variations observed under illumination in this work can provide useful evidence for the interfacial charge-transfer behavior of the $ZnIn_2S_4$/Ti_3CN heterojunction. In the C 1s spectra (Fig. 4 (a)), the deconvoluted peaks correspond to C–Ti, C–Ti–O, C–C, C–O/C–N, and C═O bonds.

Notably, the C–Ti signal in the composite is significantly attenuated compared to pristine Ti_3CN, which is ascribed to the physical shielding of the MXene surface by the intimately anchored $ZnIn_2S_4$ nanoflowers. Detailed analysis reveals that the C–Ti and C–Ti–O peaks exhibit distinct negative binding energy shifts from 282.2 eV and 283.0 eV to 281.9 eV and 282.9 eV, respectively. These modulations are synchronized with the positive shifts observed in the Zn 2p (Fig. 4 (b)), In 3d (Fig. 4 (c)), and S 2p (Fig. 4 (d)) orbitals relative to pristine $ZnIn_2S_4$. Specifically, the Zn $2p_{3/2}$ and $2p_{1/2}$ peaks shift from 1022.0 eV and 1045.0 eV to 1022.1 eV and 1045.1 eV, while the S $2p_{3/2}$ and $2p_{1/2}$ signals move from 161.6 eV and 162.8 eV to 161.9 eV and 163.1 eV, respectively. Additionally, the Ti–N peak in the N 1s spectra (Fig. 4 (e)) shifts negatively from 397.1 eV to 396.8 eV. Such a consistent redistribution of binding energies confirms strong interfacial electronic coupling, signaling a spontaneous electron flow from $ZnIn_2S_4$ to the Ti_3CN matrix.

The directional nature of this migration was further corroborated by in-situ light-irradiated XPS analysis. Upon illumination, the C–Ti and C–Ti–O peaks undergo an additional negative displacement to 281.7 eV and 282.6 eV, respectively, while the Zn 2p peaks intensify their positive shift to 1022.6 eV and 1045.6 eV. Similar intensified shifts are observed for In 3d (to 445.2 eV and 452.8 eV) and S 2p (to 162.0 eV and 163.2 eV). These dynamic responses confirm that photoexcited electrons are effectively extracted from $ZnIn_2S_4$ and injected into Ti_3CN, which acts as a robust electron sink.

To resolve the peak overlap between Ti 2p and In $3d_{3/2}$ in the optimized composite (Fig. 3 (f)), a high-loading (50%) "Enhanced" sample was further analyzed (Fig. 4). The Ti–C/Ti–N $2p_{3/2}$ and $2p_{1/2}$ features of pristine Ti_3CN are located at 455.9 and 461.8 eV, respectively, while those of the $ZnIn_2S_4$–Ti_3CN enhanced composite are located at 455.7 and 461.6 eV, indicating slight negative shifts. Under light irradiation, these peaks further shift to 455.6 and 461.5 eV. Meanwhile, the In $3d_{3/2}$ peak shifts positively from 452.7 to 452.9 eV. Although the shift magnitude is small, these coordinated changes are consistent with interfacial electronic interaction and photoinduced electron transfer from $ZnIn_2S_4$ to Ti_3CN.

3.2. *BET analysis of $ZnIn_2S_4$–Ti_3CN system*

Meanwhile, the BET analysis (Fig. S3 and Table S1) shows that $ZnIn_2S_4$, Ti_3CN MXene, and their composite ($ZnIn_2S_4$–Ti_3CN) exhibit type-IV adsorption-desorption isotherms. Compared to pristine $ZnIn_2S_4$, the $ZnIn_2S_4$–Ti_3CN composite has a slightly reduced BET surface area but remains higher than that of Ti_3CN MXene. This is due to the tight interfacial heterostructure between $ZnIn_2S_4$ and Ti_3CN, which optimizes the material's surface structure and increases the contact area with water molecules, enhancing ion adsorption and diffusion. Further details are provided in the supplementary materials. The detailed nitrogen

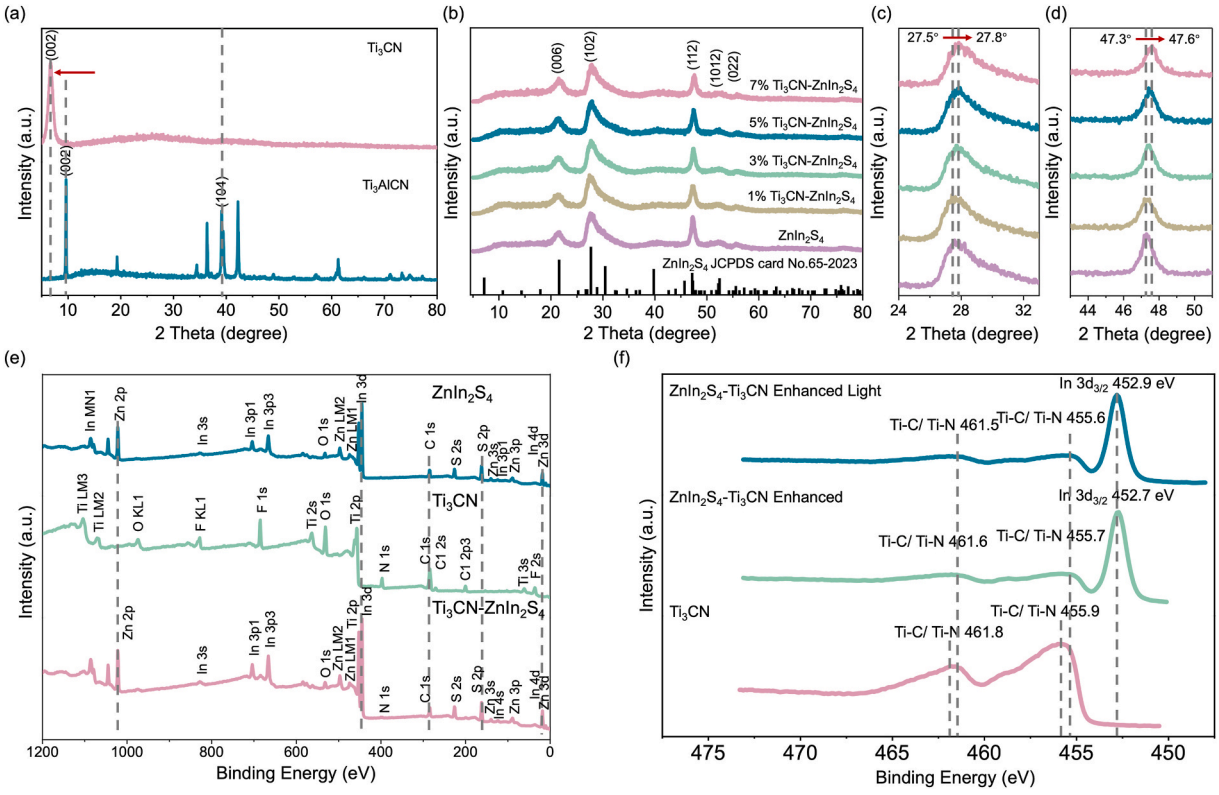

Fig. 3. (a) XRD patterns of Ti_3AlCN, Ti_3CN; (b) x- $ZnIn_2S_4$–Ti_3CN (x = 0, 1, 3, 5 and 7%) and (c-d) Enlarged partial view of; (e) XPS survey spectra of $ZnIn_2S_4$, Ti_3CN and $ZnIn_2S_4$–Ti_3CN composite; (f) High resolution XPS spectra of Ti 2p and In $3d_{3/2}$ in Ti_3CN and $ZnIn_2S_4$–Ti_3CN Enhanced composite.

adsorption-desorption isotherms and corresponding pore structure parameters are also provided in Fig. S3 and Table S1 of the Supporting Information, accompanied by the specific apparatus and computational details.

3.3. *Photocatalytic hydrogen evolution performance and mechanism study of $ZnIn_2S_4$–Ti_3CN system*

Under visible light irradiation, a comparative analysis of the photocatalytic hydrogen production performance between pure $ZnIn_2S_4$ and $ZnIn_2S_4$–Ti_3CN series catalysts was conducted. As shown in Fig. 5(a–b), compared with pure $ZnIn_2S_4$, $ZnIn_2S_4$–Ti_3CN composites with different Ti_3CN contents exhibited significantly improved photocatalytic hydrogen production performance. Among them, 3% Ti_3CN– $ZnIn_2S_4$ showed the optimal activity, with a hydrogen production rate of 603.3 μmol g^{-1} h^{-1}, which is 2.4 times that of pure $ZnIn_2S_4$ (254.0 μmol g^{-1} h^{-1}), so "$ZnIn_2S_4$–Ti_3CN" refers to the optimized sample containing 3 wt% Ti_3CN, consistent with the definition already given in the *Experimental section*. This enhancement is mainly attributed to the addition of Ti_3CN, which effectively reduces the recombination of photogenerated carriers, hence improving the photocatalytic hydrogen production efficiency. However, with further increase in Ti_3CN content, the photocatalytic activity decreases due to the light-shielding effect. After four consecutive 5 h cycles under visible-light irradiation (20 h in total), the 3 wt% $Ti_3CN/ZnIn_2S_4$ composite maintained stable H_2-evolution performance, indicating good stability and reusability (Fig. 5 (c)). In addition, the effect of different catalyst masses on hydrogen production efficiency was investigated (Fig. 5 (d)). The correlation between photocatalyst dosage and hydrogen evolution efficiency was systematically investigated. The results indicate that the hydrogen production rate increases almost linearly when the catalyst mass is maintained below 20 mg. However, as the dosage reaches 150 mg, the catalytic activity gradually plateaus, primarily due to the light-shielding effect where excessive catalyst particles impede effective light penetration and scattering within the suspension. Furthermore, the apparent quantum efficiency (AQE) was determined as a critical metric to evaluate the solar-to-chemical energy conversion capability. As a paramount indicator of photocatalytic performance, AQE provides essential theoretical guidance for assessing the feasibility of these materials in practical large-scale applications.

In this experiment, the AQE of 100 mg catalyst was tested at different wavelengths (Fig. 5 (e)). It was found that the quantum efficiency is positively correlated with the light absorption capacity. Especially under 350 nm monochromatic light irradiation, the AQE of $ZnIn_2S_4$–Ti_3CN composite reaches 1.4%.

The light-harvesting capabilities of the as-prepared photocatalysts, which fundamentally dictate their solar energy conversion efficiency, were evaluated via ultraviolet-visible diffuse reflectance spectroscopy (UV-Vis DRS). All samples exhibit a broad absorption response spanning from the UV to the visible region. Compared to pristine $ZnIn_2S_4$, which shows relatively moderate visible-light absorption, the introduction of Ti_3CN MXene significantly enhances the optical absorption intensity. Specifically, as the Ti_3CN content increases, the $ZnIn_2S_4$–Ti_3CN composites demonstrate a progressively extended photoresponse range and heightened absorbance across the visible spectrum. This optical enhancement is primarily ascribed to the narrow bandgap and the characteristic metallic nature of the Ti_3CN MXene matrix.

Beyond intensifying light harvesting, the 2D architectural merits and superior metallic conductivity of Ti_3CN facilitate the creation of high-speed channels for the separation and migration of photogenerated carriers. This synergistic effect not only optimizes the utilization of incident photons but also increases the density of accessible surface active sites by promoting the efficient export of photogenerated electrons. Consequently, the UV-Vis DRS analysis not only elucidates the intrinsic optical properties of the heterojunction but also serves as a critical indicator of its potential photocatalytic activity, providing essential insights for the rational design of high-performance composite catalysts.

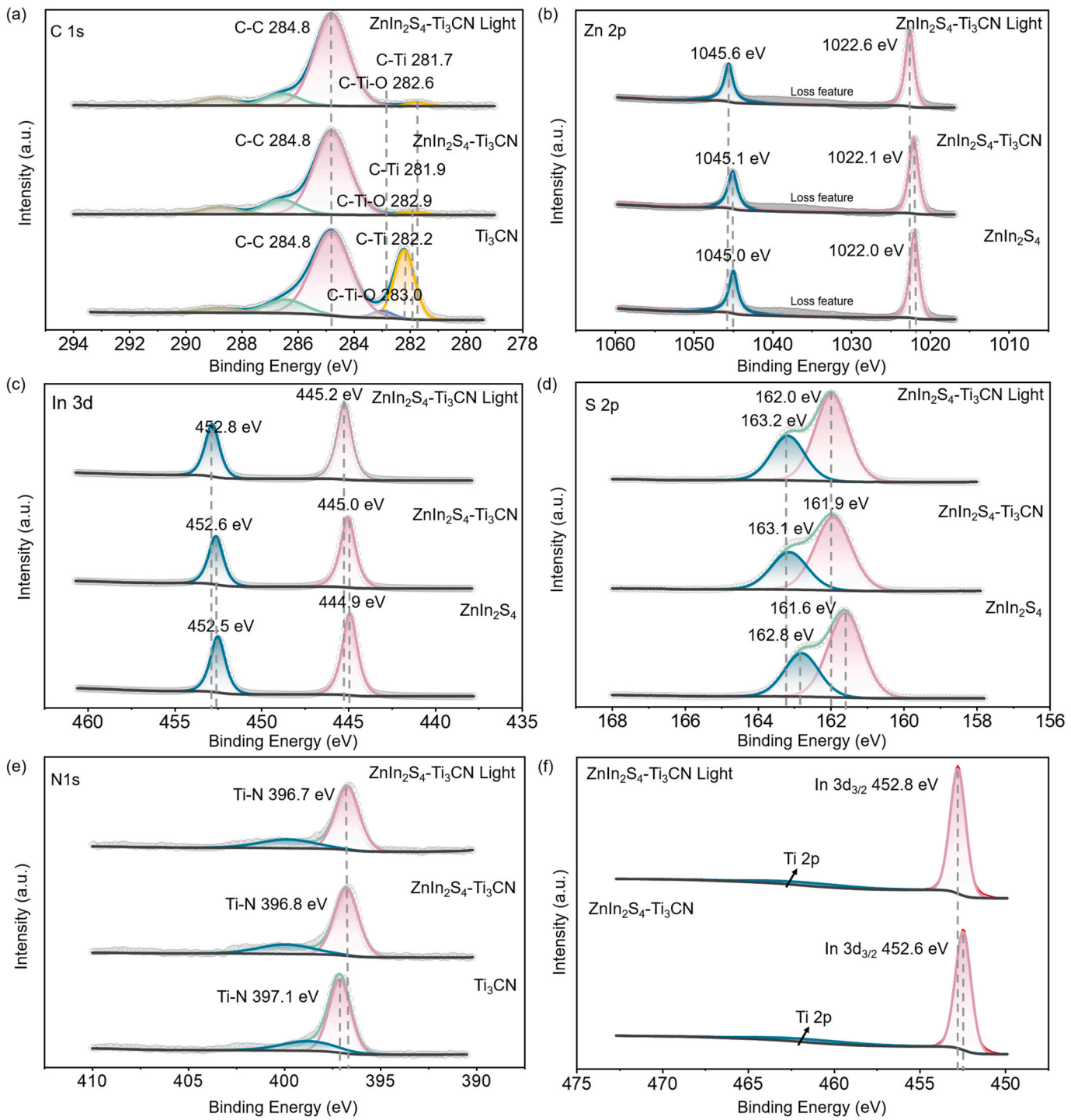

Fig. 4. High resolution XPS spectra of (a) C 1s, (b) Zn 2p, (c) In 3 d, (d) S 2p, (e) N 1s and (f) Ti 2p and In $3d_{3/2}$.

Fig. 5(f–h) shows the electron paramagnetic resonance (EPR) spectra of $ZnIn_2S_4$ and $ZnIn_2S_4$–Ti_3CN using TEMPO as the trapping agent under dark and light irradiation conditions. TEMPO is a nitroxide radical probe with a characteristic EPR signal. Under light irradiation, photogenerated electrons can reduce TEMPO to an EPR-silent or much less EPR-active species, such as TEMPOH, resulting in the attenuation of the TEMPO signal [52,53]. Under dark conditions, $ZnIn_2S_4$ and $ZnIn_2S_4$–Ti_3CN show comparable EPR signal intensities, indicating that no obvious TEMPO reduction occurs in the absence of light. After 5 min of light irradiation, the EPR signal of $ZnIn_2S_4$–Ti_3CN becomes weaker than that of pure $ZnIn_2S_4$, suggesting that more photoinduced electrons are available to participate in the reduction of TEMPO in the composite system. As the irradiation time is extended to 10 min, the EPR signals of both samples further decrease, while $ZnIn_2S_4$–Ti_3CN still exhibits a more pronounced signal attenuation than pristine $ZnIn_2S_4$. This result indicates that the $ZnIn_2S_4$–Ti_3CN composite possesses more efficient photoinduced electron generation and transfer ability, which is consistent with its enhanced photocatalytic H_2 evolution performance.

3.4. *Optical and photo-electrochemical properties*

The efficacy of photocatalytic hydrogen evolution is fundamentally

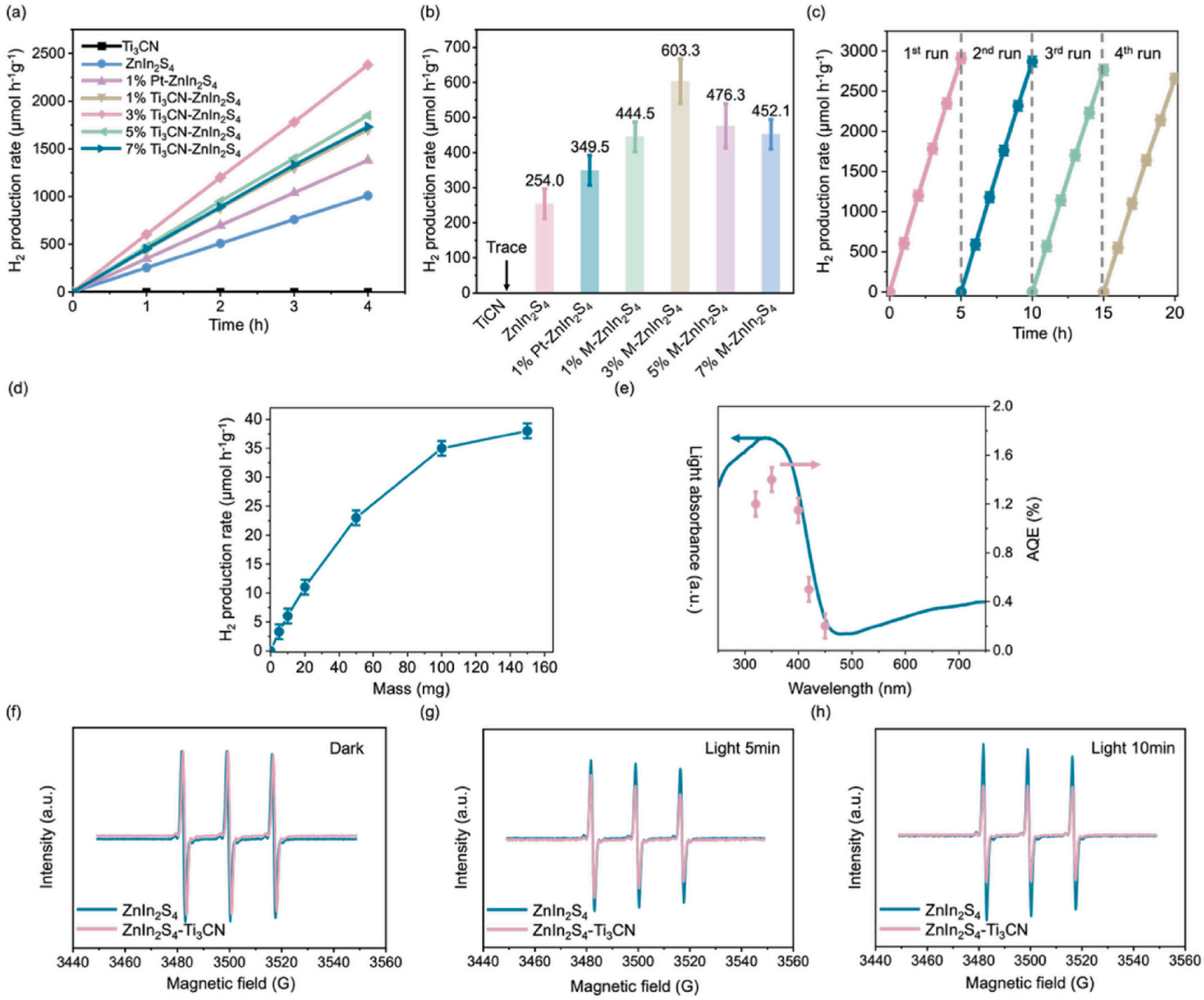

Fig. 5. Photocatalytic activity analysis: (a) Time-dependent photocatalytic hydrogen generation of $ZnIn_2S_4$–Ti_3CN composites with different Ti_3CN contents; (b) Comparative graph of average photocatalytic hydrogen production rates for $ZnIn_2S_4$–Ti_3CN composites with various Ti_3CN contents; (c) Cyclic stability test of the 3 wt% $ZnIn_2S_4$–Ti_3CN photocatalyst over four consecutive 5 h cycles (20 h total irradiation). (d) Photocatalytic hydrogen production rates of $ZnIn_2S_4$–Ti_3CN composite materials at different masses; (e) Apparent quantum efficiency (AQE) of $ZnIn_2S_4$–Ti_3CN composite; (f) EPR signals of TEMPO as the electron-trapping agent for $ZnIn_2S_4$ and $ZnIn_2S_4$–Ti_3CN under dark conditions; (g) EPR signals of TEMPO as the electron-trapping agent for $ZnIn_2S_4$ and $ZnIn_2S_4$–Ti_3CN after 5 min of light irradiation; (h) EPR signals of TEMPO as the electron-trapping agent for $ZnIn_2S_4$ and $ZnIn_2S_4$–Ti_3CN after 10 min of light irradiation.

dictated by the generation, spatial separation, and transfer kinetics of photogenerated charge carriers. To comprehensively evaluate these dynamic processes, experimental techniques such as transient photocurrent response, electrochemical impedance spectroscopy (EIS), and photoluminescence (PL) spectroscopy were systematically employed. In the comparative analysis, the $ZnIn_2S_4$–Ti_3CN composite exhibited a stronger photocurrent response than pure $ZnIn_2S_4$ (as shown in Fig. 6 (a)), which reveals that charge carriers are separated more efficiently in the composite [54]. Furthermore, the EIS of $ZnIn_2S_4$– Ti_3CN (see in Fig. 6 (b)) showed a smaller semicircle diameter compared with pure $ZnIn_2S_4$, indicating that the composite has lower charge transfer impedance, thereby promoting efficient charge transport [55]. It can be seen from Fig. 6(c–d) that after adding Ti_3CN, the photoluminescence intensity of $ZnIn_2S_4$–Ti_3CN is significantly reduced, which indicates that the introduction of Ti_3CN effectively inhibits the recombination of electron-hole pairs [56]. In conclusion, Ti_3CN plays a crucial role in promoting the separation and transport of photogenerated electrons, thereby significantly enhancing its photocatalytic hydrogen production performance.

To elucidate the origins of the varied photocatalytic activities, the light-harvesting capabilities of the synthesized samples were investigated via UV-Vis diffuse reflectance spectroscopy (DRS) (Fig. 6 (e)). While pristine $ZnIn_2S_4$ exhibits a restricted visible-light response, the $ZnIn_2S_4$–Ti_3CN composites display a progressively broadened and intensified absorption profile across the visible spectrum with increasing MXene content. This optical enhancement is inherently governed by the exceptional visible-light harvesting characteristics of the Ti_3CN matrix. Crucially, beyond maximizing photon capture, the highly conductive 2D architecture of Ti_3CN establishes high-speed channels for the separation and migration of photogenerated carriers while simultaneously exposing abundant surface active sites. Therefore, the integration of Ti_3CN synergistically optimizes both incident light utilization and charge transfer dynamics, fundamentally underpinning the superior hydrogen evolution performance of the composite system.

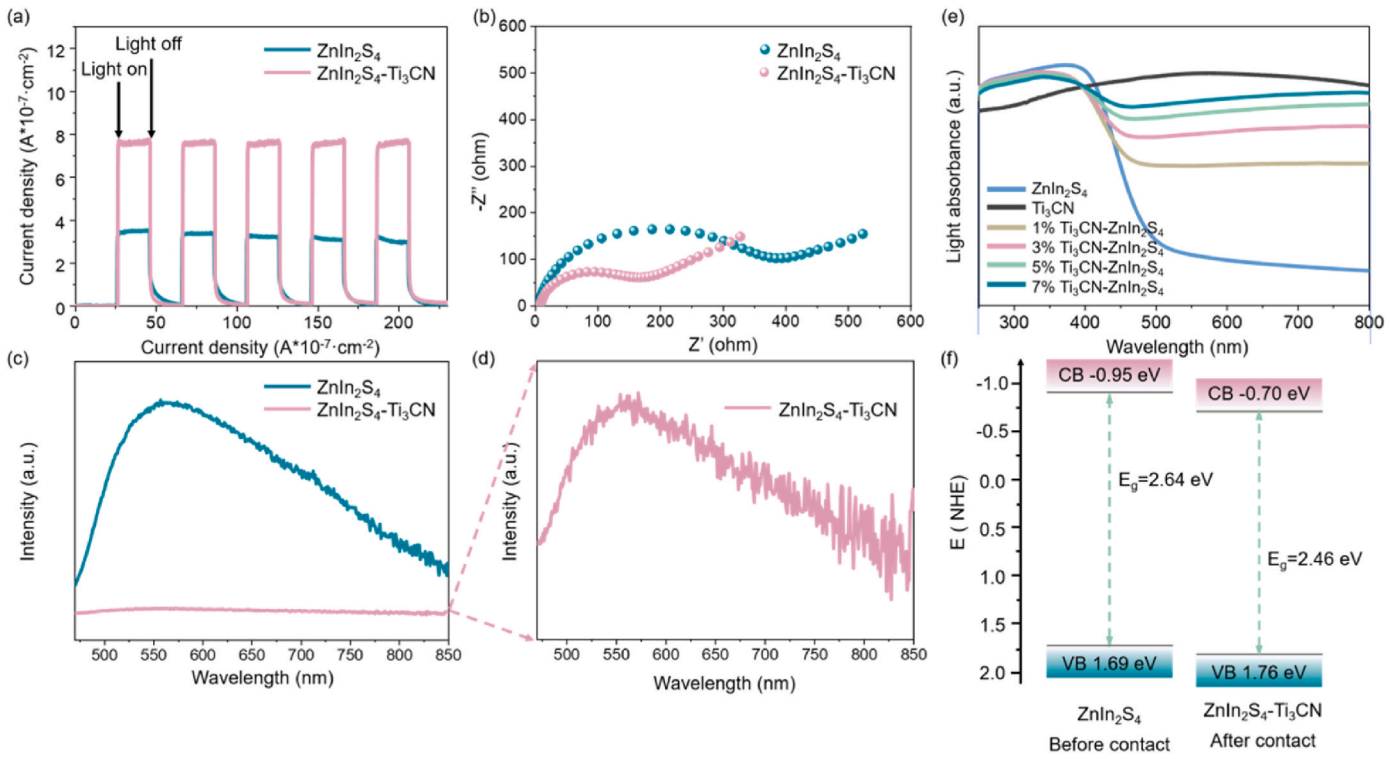

Fig. 6. $ZnIn_2S_4$ and $ZnIn_2S_4$–Ti_3CN: (a) Photocurrent responses; (b) EIS Nyquist plots; (c) Photoluminescence (PL) spectra and (d) PL of single $ZnIn_2S_4$–Ti_3CN sample; (e) UV-visible diffuse reflectance spectra of different samples; (f) Schematic illustration of band structures of $ZnIn_2S_4$ before contact and $ZnIn_2S_4$–Ti_3CN after contact.

Based on the energy band alignment analysis shown in Fig. 6 (f), the conduction band (CB) and valence band (VB) positions of $ZnIn_2S_4$ before and after contact with Ti_3CN are compared. Before the contact, the CB of $ZnIn_2S_4$ is positioned at −0.95 eV, with a bandgap (Eg) of 2.64 eV, and the VB is at 1.69 eV. After forming the $ZnIn_2S_4$–Ti_3CN heterojunction, the CB shifts to −0.70 eV, with the bandgap decreasing to 2.46 eV, while the VB increases to 1.76 eV. This shift in the energy band structure indicates the formation of a staggered type heterojunction, which is beneficial for enhancing charge separation and transport, providing a more favorable environment for photocatalytic hydrogen production. The potential alignment and bandgap narrowing are thermodynamically favorable for efficient photocatalysis, supporting the feasibility of the composite for enhanced hydrogen evolution performance under visible light.

3.5. *Theoretical calculation and possible photocatalytic mechanism*

To deeply investigate the interfacial electron transfer characteristics between $ZnIn_2S_4$ and Ti_3CN MXene, a comprehensive analysis of the energy level structure of the $ZnIn_2S_4$–Ti_3CN heterojunction was performed. The work function of the samples was measured by ultraviolet photoelectron spectroscopy (UPS), as shown in Fig. 7(a–c). To ensure accuracy, we first calibrated the Fermi edge using the UPS spectrum of a gold (Au) substrate treated by argon (Ar) ion sputtering. This step ensured that the reference zero point of the binding energy of all UPS spectra was set based on this calibration point. The formula for calculating the work function (Φ) is: $\Phi = h\nu - (E_{cut\ off} - E_{Fermi})$, where $h\nu$ is the incident photon energy (21.22 eV), $E_{cut\ off}$ is the binding energy of the cut-off edge, and E_{Fermi} is the Fermi edge, set to 0 eV [57]. Based on this, the cut-off edge binding energies of $ZnIn_2S_4$, Ti_3CN MXene, and $ZnIn_2S_4$–Ti_3CN composite obtained from Fig. 7(a–c) are 17.15 eV, 16.64 eV, and 16.92 eV, respectively, and the calculated work functions are 4.07 eV, 4.58 eV, and 4.30 eV, respectively. The valence band (VB) position was measured by valence band XPS spectrum (Fig. 7(d–e)). Using formulas $E_{NHE} = \Phi + 1.63 - 4.44$ and $E_{NHE} = \Phi + 1.70 - 4.44$, the valence band potentials of $ZnIn_2S_4$ and $ZnIn_2S_4$–Ti_3CN were calculated to be 1.69 eV and 1.76 eV, respectively [58]. The band gaps of $ZnIn_2S_4$ and $ZnIn_2S_4$–Ti_3CN measured by the Kubelka-Munk method (Fig. 7(f–g)) are 2.64 eV and 2.46 eV, respectively [58,59]. Calculated based on formula ($E_{CB} = E_{VB} - E_g$), the conduction band positions of $ZnIn_2S_4$ and $ZnIn_2S_4$–Ti_3CN are −0.95 eV and −0.70 eV, respectively. It should be noted that the work function obtained from UPS is inherently surface-sensitive, especially for a composite sample, and may therefore be influenced by the surface-exposed component, local interfacial coverage, and surface terminations. Accordingly, the measured work function of the $ZnIn_2S_4$–Ti_3CN composite is interpreted here as an effective near-surface electronic parameter rather than an absolute bulk value. Nevertheless, the proposed interfacial energy-level diagram is supported by the consistent trends obtained from UPS, valence-band XPS, in-situ XPS, and DFT calculations, which collectively indicate electron transfer from $ZnIn_2S_4$ to Ti_3CN and the upward band bending of $ZnIn_2S_4$ after contact.

Based on the above experimental and theoretical results, Fig. 7 (h) schematically summarizes the interfacial energy-level alignment of the $ZnIn_2S_4$–Ti_3CN heterojunction. Due to its lower work function and higher Fermi level, $ZnIn_2S_4$ shows an obvious tendency of electron migration to Ti_3CN MXene compared with Ti_3CN MXene. This is further verified by the positive shift of the binding energy of the In 3d peak (Fig. 7(d–e)), proving that electrons are indeed transferred from $ZnIn_2S_4$ to Ti_3CN MXene. When $ZnIn_2S_4$ is in contact with Ti_3CN MXene, the Fermi levels of the two converge and reach the same level. Moreover, the energy band of $ZnIn_2S_4$ bends upward after contact with Ti_3CN MXene, which effectively inhibits the backflow of electrons and promotes the effective separation of photogenerated electrons and holes, providing favorable conditions for improving the photocatalytic hydrogen production performance [60,61].

Fig. 8(a–c) present the structural models of $ZnIn_2S_4$, Ti_3CN MXene, and the $ZnIn_2S_4$–Ti_3CN composite formed by these two components. Subsequent calculations of the band structures of these materials (see in Fig. 8(d–f)) reveal that $ZnIn_2S_4$ exhibits typical semiconductor

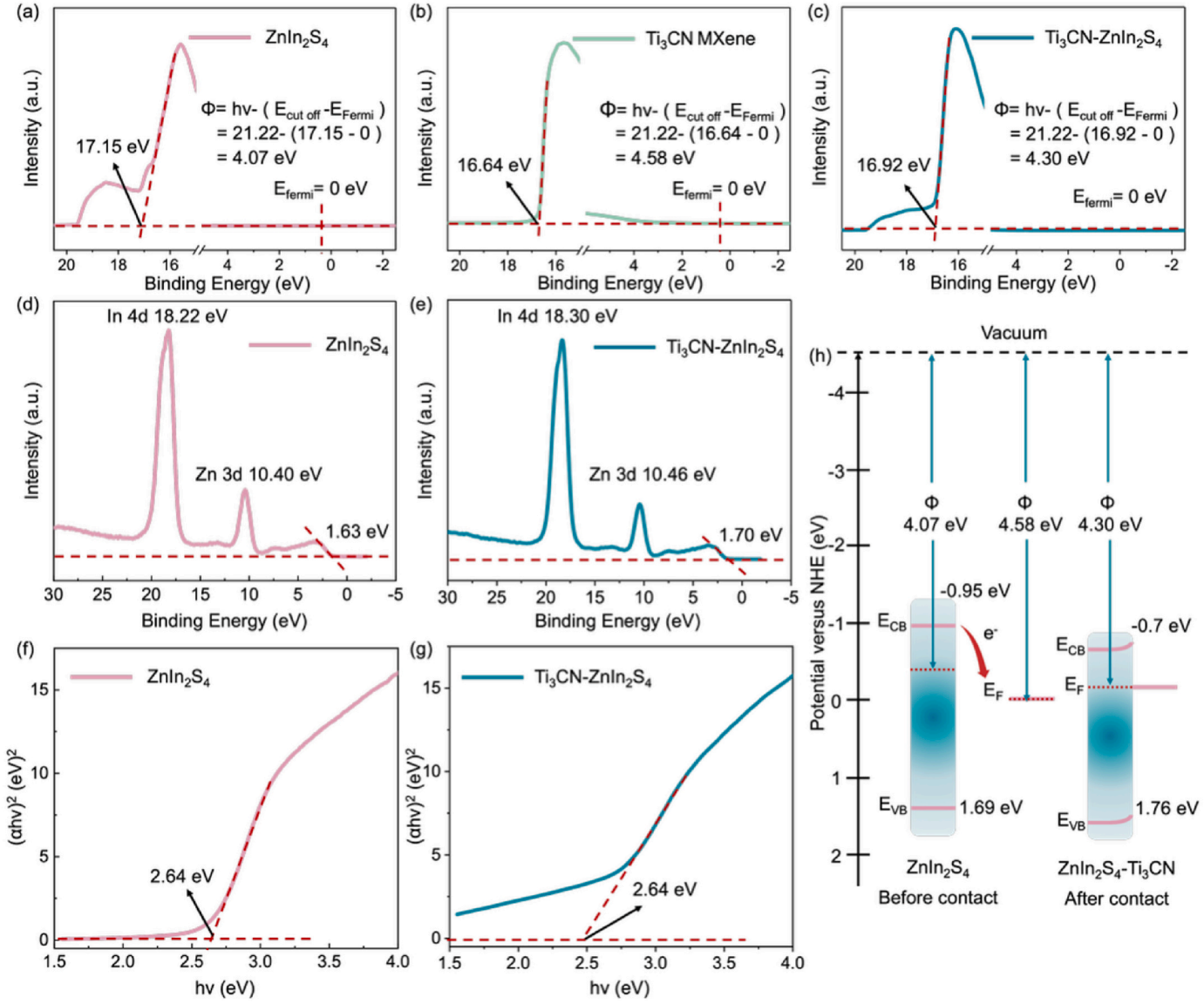

Fig. 7. UPS and band structure analysis: (a-c) UPS spectra of $ZnIn_2S_4$, Ti_3CN MXene, and $ZnIn_2S_4$–Ti_3CN; (d-e) Valence band XPS spectra of $ZnIn_2S_4$ and $ZnIn_2S_4$–Ti_3CN; (f) Tauc plots for band gap of $ZnIn_2S_4$ and $ZnIn_2S_4$–Ti_3CN; (g) Schematic illustration of band structure for $ZnIn_2S_4$, Ti_3CN MXene, and $ZnIn_2S_4$–Ti_3CN composites. (h) Schematic illustration of the interfacial band alignment and charge-transfer pathway in the $ZnIn_2S_4$/Ti_3CN heterojunction.

characteristics. After compositing with Ti_3CN MXene, the band gap of the composite narrows—this indicates enhanced light absorption intensity, which is consistent with the earlier experimental results on band structure. Additionally, the band structure of the composite becomes dense and smooth, suggesting improved electrical conductivity [62]. Meanwhile, the density of states (DOS) of $ZnIn_2S_4$, Ti_3CN MXene, and the $ZnIn_2S_4$–Ti_3CN composite was analyzed (Fig. 8(g–i)). The conduction band of the composite is primarily composed of Ti orbitals, demonstrating that the active sites are located on Ti atoms. To further clarify the electron migration process within the composite, the differential charge density distribution at the interface of the $ZnIn_2S_4$–Ti_3CN composite was simulated.

The top view and front view (Fig. 9(a–b)) clearly illustrate electron accumulation on the Ti_3CN side (yellow regions) and electron depletion on the $ZnIn_2S_4$ side (blue regions), which is a clear indication of electron migration from $ZnIn_2S_4$ to Ti_3CN. Furthermore, the plane-averaged differential charge density plot (Fig. 9 (c)) provides additional evidence for dynamic electron transfer under light irradiation. At the interface between $ZnIn_2S_4$ and Ti_3CN, the negative value on the $ZnIn_2S_4$ side reflects electron consumption on its surface, while the positive value on the Ti_3CN side indicates electron accumulation on its surface. This confirms that electrons are mainly transferred from $ZnIn_2S_4$ to Ti_3CN MXene. Further analysis of the Gibbs free energy of hydrogen atom adsorption (Fig. 9(d–f)) shows that the ΔG_{H^*} value of the $ZnIn_2S_4$–Ti_3CN composite is −0.21 eV, compared with −0.38 eV for pure $ZnIn_2S_4$. The ΔGH* value of the $ZnIn_2S_4$–Ti_3CN composite is closer to zero than that of pure $ZnIn_2S_4$, meaning the composite has a lower overpotential and is more conducive to hydrogen production.

In addition, theoretical calculations were conducted to analyze the cross-sectional work functions of $ZnIn_2S_4$, Ti_3CN MXene, and the $ZnIn_2S_4$–Ti_3CN composite, which were determined to be 5.63 eV, 6.16 eV, and 5.95 eV, respectively (Fig. 10(a–c)). This result shows that the higher work function of Ti_3CN MXene drives electrons to migrate from $ZnIn_2S_4$ to Ti_3CN MXene. The convergence of work functions causes the energy band of $ZnIn_2S_4$ to bend upward, which facilitates the effective separation of electron-hole pairs and thereby enhances the efficiency of photocatalytic water splitting for hydrogen production.

Moreover, theoretical calculations were used to conduct an in-depth

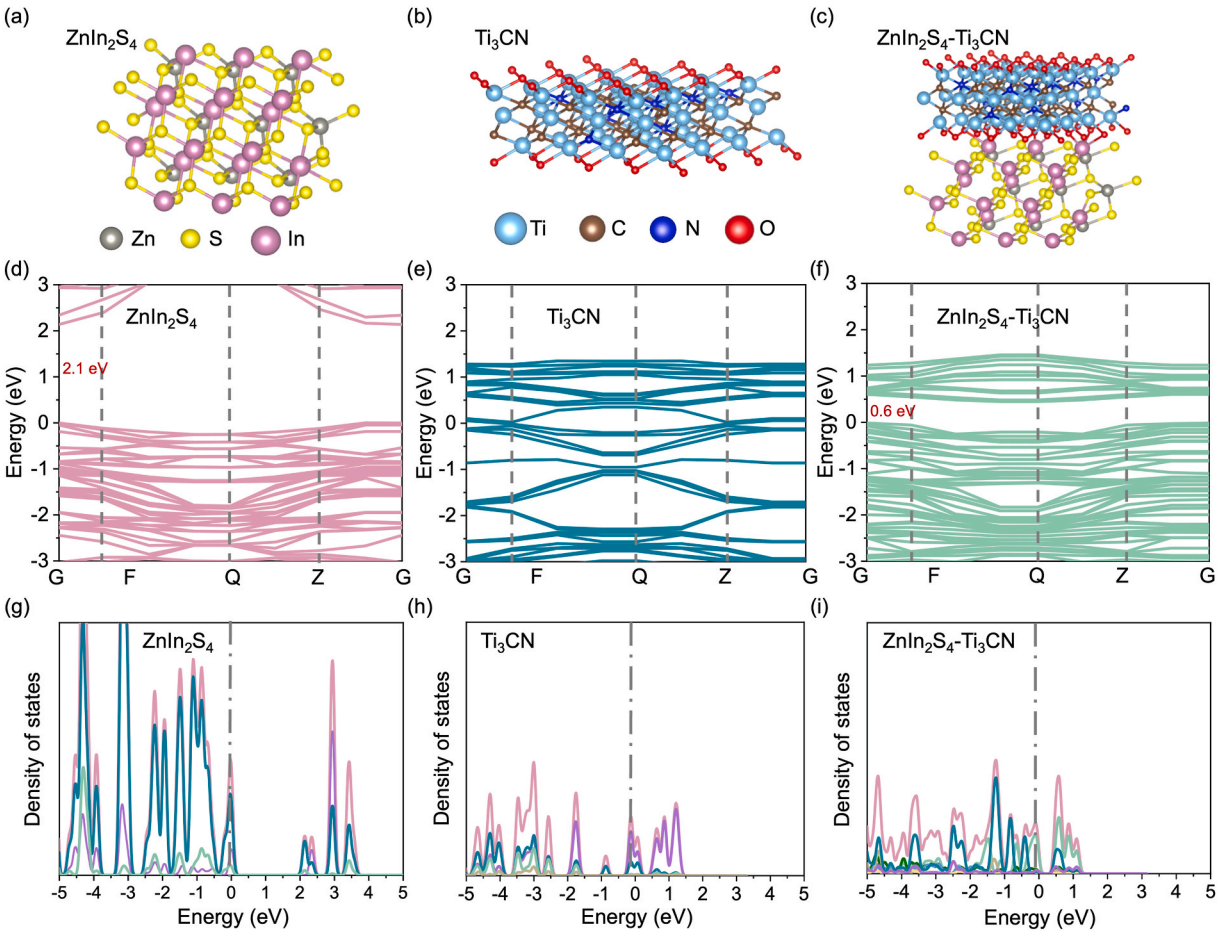

Fig. 8. Schematic structure models (a-c), Energy band structure (d-f) and Density of states (g-i) of $ZnIn_2S_4$, Ti_3CN and $ZnIn_2S_4$–Ti_3CN.

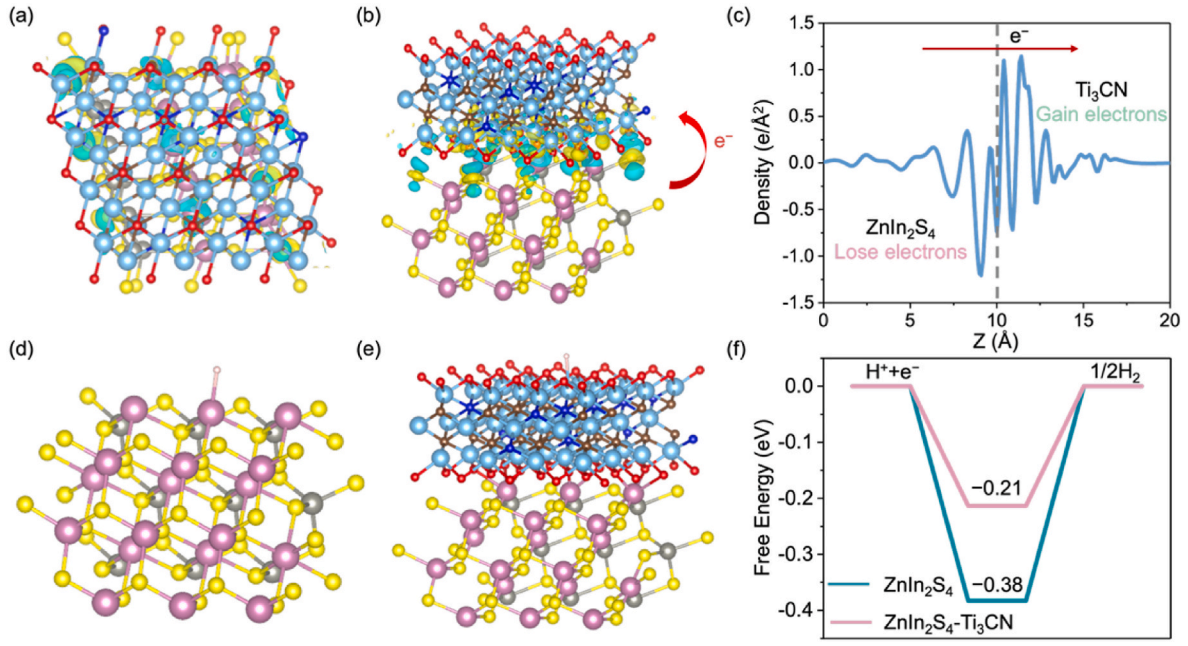

Fig. 9. Charge transfer and hydrogen adsorption analysis: Top and side views of charge density difference for $ZnIn_2S_4$-MXene composite (a, b), Planar-averaged electron density difference along Z-direction (c), with hydrogen adsorption structure models for $ZnIn_2S_4$ (d) and $ZnIn_2S_4$–Ti_3CN (e), and free energy diagrams of photocatalytic hydrogen evolution for $ZnIn_2S_4$ and $ZnIn_2S_4$–Ti_3CN (f).

investigation of the reaction mechanism of $ZnIn_2S_4$ and its composite with Ti_3CN during water adsorption and decomposition. As shown in

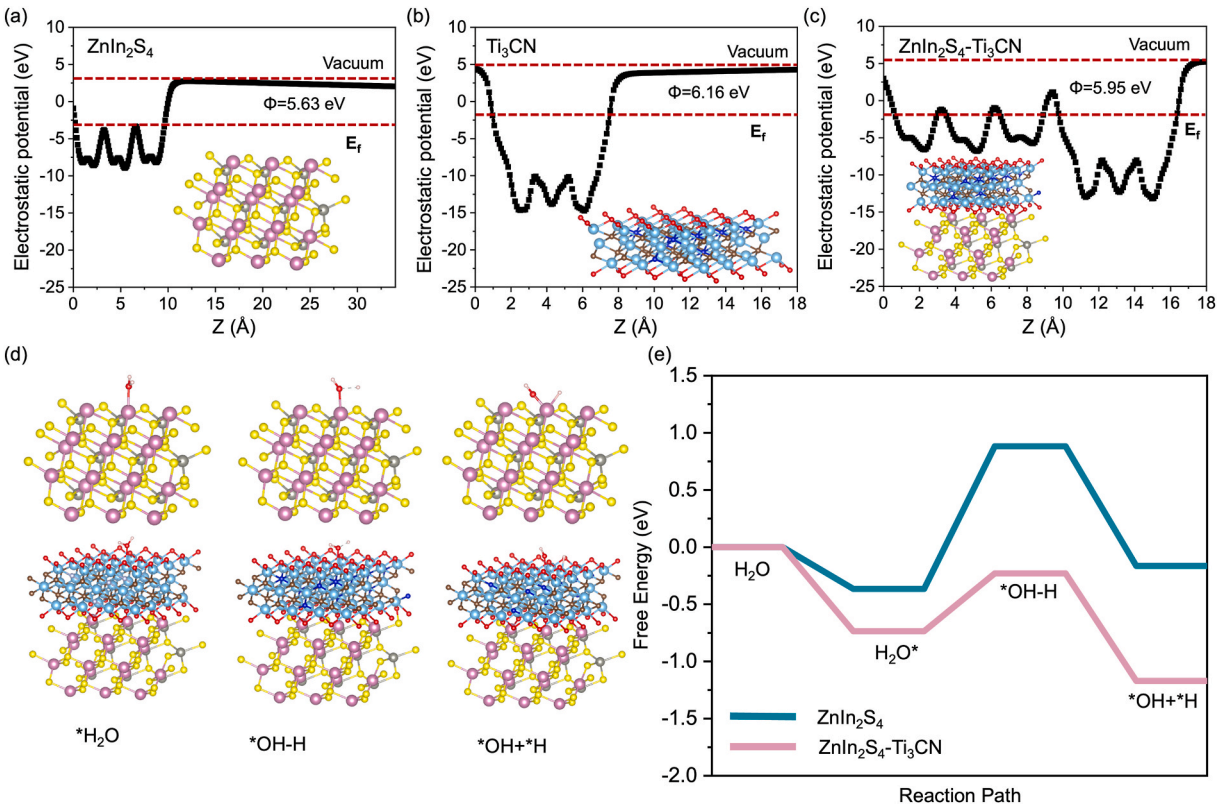

Fig. 10. Electrostatic potentials of the (a) $ZnIn_2S_4$, (b) Ti_3CN, and the (c) $ZnIn_2S_4$–Ti_3CN (Inserted: the correspond crystal structures of samples); (d) Structural models of water adsorption and decomposition stages for $ZnIn_2S_4$ and $ZnIn_2S_4$–Ti_3CN; (e) Free energy diagrams of the whole hydrolysis process on photocatalysts.

Fig. 10 (d), detailed structural models of pure $ZnIn_2S_4$ and the $ZnIn_2S_4$–Ti_3CN composite during the water adsorption and decomposition stages are provided. Additionally, the Gibbs free energy changes of these two materials during the water splitting reaction were

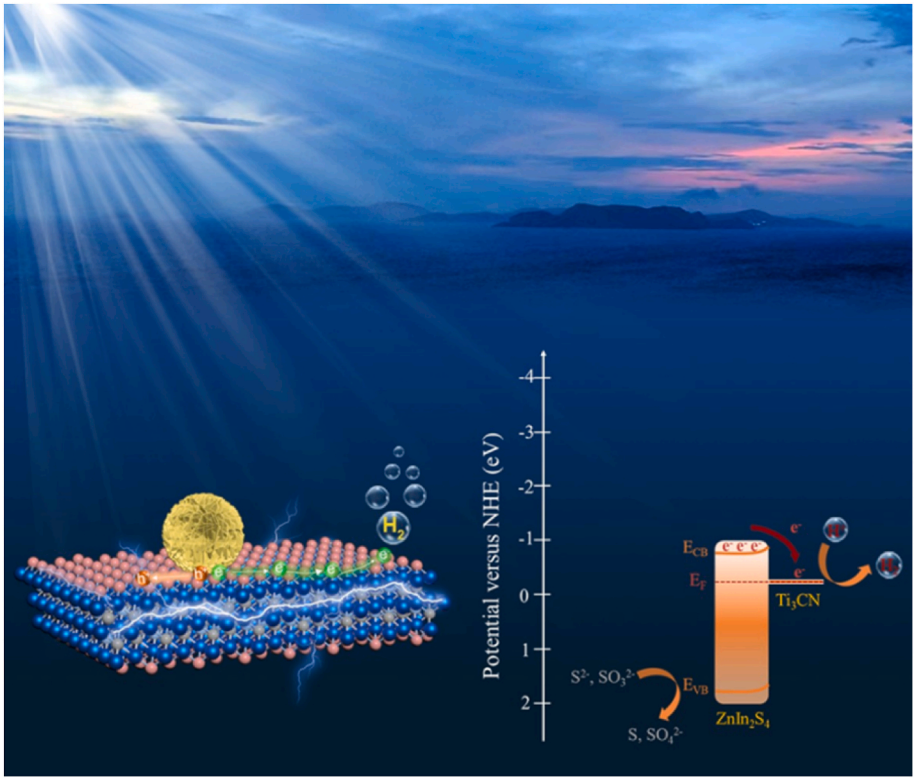

Fig. 11. Schematic illustration of the photocatalytic H_2 production mechanism of $ZnIn_2S_4$–Ti_3CN.

calculated and analyzed (Fig. 10 (e)) to evaluate their catalytic efficiency. The results indicate that the $ZnIn_2S_4$–Ti_3CN composite has a lower energy barrier than pure $ZnIn_2S_4$ in promoting the water splitting reaction, which means the composite can decompose water molecules more efficiently and thus improve catalytic hydrogen production performance. Furthermore, the free energies of the adsorbed states of *OH and *H are lower than that of the adsorbed state of water, which further confirms that the $ZnIn_2S_4$–Ti_3CN composite can facilitate the complete water splitting process.

DFT calculations provide a robust theoretical foundation that extends beyond experimental validation to reveal the intrinsic mechanisms of enhanced activity. By simulating the $ZnIn_2S_4$–Ti_3CN interface, we substantiate that the MXene matrix fundamentally reconfigures the charge distribution, creating an energetically favorable environment for carrier separation. Crucially, the theoretical model identifies a significantly reduced overpotential, confirming that Ti_3CN not only serves as a conductive mediator but also lowers the thermodynamic barrier for proton reduction. This synergy between theoretical insights and experimental evidence confirms that the rational design of this hierarchical heterostructure is the key driver of superior solar-to-hydrogen conversion. Collectively, the charge transfer dynamics and catalytic pathways within the $ZnIn_2S_4$–Ti_3CN composite were systematically elucidated through a comprehensive integration of XPS, UPS, in-situ XPS, DFT calculations, and photoelectrochemical analyses (Fig. 11). Under solar irradiation, electrons in $ZnIn_2S_4$ are excited to the conduction band and rapidly migrate to the intimately coupled Ti_3CN MXene nanosheets, triggering the reduction of surface-adsorbed protons (H^+) into H_2. Concurrently, the remaining photogenerated holes in the $ZnIn_2S_4$ valence band are efficiently consumed by the sacrificial agent. Beyond merely acting as a highly conductive electron sink to accelerate charge transport, the Ti_3CN matrix fundamentally dictates the interfacial energetics. Specifically, the Fermi-level equilibration between the two components induces an upward band bending within $ZnIn_2S_4$, creating a robust interfacial built-in electric field. This directional driving force effectively suppresses electron backflow and mitigates severe carrier recombination, ultimately maximizing the overall photocatalytic hydrogen evolution efficiency.

4. Conclusion

In conclusion, a novel $ZnIn_2S_4$/Ti_3CN MXene heterojunction was successfully engineered via a facile in-situ self-assembly strategy. The resulting hierarchical architecture achieves a peak hydrogen evolution rate of 603.3 μmol g^{-1} h^{-1} with an optimized 3% Ti_3CN loading, representing a 2.4-fold increase over pristine $ZnIn_2S_4$ (254.0 μmol g^{-1} h^{-1}) while maintaining robust stability and reusability. Experimental and computational results substantiate that the intimate interfacial coupling establishes high-speed charge transfer channels, where the metallic Ti_3CN functions as an efficient electron conductor to rapidly extract and transfer photoexcited electrons from $ZnIn_2S_4$ for proton reduction. Crucially, Fermi-level equilibration at the interface induces upward band bending and a robust built-in electric field within $ZnIn_2S_4$, providing a directional driving force that effectively suppresses electron backflow and carrier recombination. Furthermore, DFT calculations confirm that the introduction of Ti_3CN significantly lowers the reaction overpotential and thermodynamic energy barriers during the photocatalytic water splitting process, thereby favoring H_2 generation. Overall, this work provides a new paradigm and mechanistic guidance for the rational design of MXene-assisted heterojunction systems toward highly efficient solar energy conversion.

CRediT authorship contribution statement

Yakun Song: Investigation, Validation, Writing – original draft. **Huajun Gu:** Conceptualization, Methodology. **Yifan Liao:** Writing – review & editing. **Jiayi Meng:** Data curation. **Yamei Huang:** Formal analysis. **Quanmei Zhou:** Validation. **Yuchen Wei:** Formal analysis. **Yuying Hu:** Validation. **Mohan Zhang:** Formal analysis. **Bite Deng:** Validation. **Wei-Lin Dai:** Funding acquisition, Project administration, Supervision, Visualization, Writing – review & editing.

Declaration of competing interest

The authors declare that they have no known competing financial interests or personal relationships that could have appeared to influence the work reported in this paper.

Acknowledgments

This work was funded by the National Key Research and Development Program of China (2021YFA1501404), and the Science and Technology Commission of Shanghai Municipality (2024ZDSYS02).

Appendix B. Supplementary data

Supplementary data to this article can be found online at https://doi.org/10.1016/j.ijhydene.2026.155902.

Data availability

Data will be made available on request.

References

[1] Yang Z, Wu J, Shang X, Fu R, Xie L, Ge Q. Scaling laws of CO_2 emissions during global urban expansion. NPJ Urban Sustainability 2025;5:3. https://doi.org/10.1038/s42949-024-00172-x.
[2] Mahdavi P, Ross L M, Simoni E. Government efforts to reduce fossil fuel subsidies have failed at a very high rate. Nat Clim Change 2025;15:471–2. https://doi.org/10.1038/s41558-025-02304-2.
[3] Zhang Z, Zhen Q, Zhu R, Zhang F, Zhong T, Lin J, Ning L, Xie W, et al. Worldwide rooftop photovoltaic electricity generation may mitigate global warming. Nat Clim Change 2025;15:393–402. https://doi.org/10.1038/s41558-025-02276-3.
[4] Sinha A, Venkatesh A, Jordan K, Wade C, Eshraghi H, de Queiroz AR, Jaramillo P, Johnson Je X. Diverse decarbonization pathways under near cost-optimal futures. Nat Commun 2024;15:8165. https://www.nature.com/articles/s41467-024-52433-z.
[5] Staadecker M, Szinai J, Sánchez-Pérez PA, Kurtz S, Hidalgo-Gonzalez P. The value of long-duration energy storage under various grid conditions in a zero-emissions future. Nat Commun 2024;15:9501. https://doi.org/10.1038/s41467-024-53274-6.
[6] Hisatomi T, Yamada T, Nishiyama H, Takata T, Domen K. Materials and systems for large-scale photocatalytic water splitting. Nat Rev Mater 2025;10:769–82. https://doi.org/10.1038/s41578-025-00823-0.
[7] Lin L, Ma Y-W, Vequizo JM, Nakabayashi M, Gu C, Tao X, Yoshida H, Pihosh Y, Nishina Y, Yamakata A, Shibata N, Hisatomi T, Takata T, Domen K. Efficient and stable visible-light-driven Z-scheme overall water splitting using an oxysulfide H_2 evolution photocatalyst. Nat Commun 2024;15:397. https://doi.org/10.1038/s41467-024-44706-4.
[8] Odenweller A, Ueckerdt F. The green hydrogen ambition and implementation gap. Nat Energy 2025;10:110–23. https://doi.org/10.1038/s41560-024-01684-7.
[9] Chen Y, Dai Ch, Wu Q, Li H, Xi Sh, Seow J Zhu Y, Luo S, Meng F, Bo Y, Xia Y, Jia Y, Fisher AC, Xu Zh J. Support-free iridium hydroxide for high-efficiency proton-exchange membrane water electrolysis. Nat Commun 2025;16:2730. https://www.nature.com/articles/s41467-025-58019-7.
[10] Du X, Ji H, Xu Y, Du S, Feng Z, Dong B, Wang R, Zhang F. Covalent organic framework without cocatalyst loading for efficient photocatalytic sacrificial hydrogen production from water. Nat Commun 2025;16:3024. https://doi.org/10.1038/s41467-025-58337-w.
[11] Chen S, Takata T, Domen K. Particulate photocatalysts for overall water splitting. Nat Rev Mater 2017;2:17050–66. https://doi.org/10.1038/natrevmats.2017.50.
[12] Li Y, Zhou H, Cai S, Prabhakaran D, Niu W, Large A, Held G, Taylor RA, Wu X-P, S. C. Edman Tsang. Electrolyte-assisted polarization leading to enhanced charge separation and solar-to-hydrogen conversion efficiency of seawater splitting. Nat Catal 2024;7:77–88. https://doi.org/10.1038/s41929-023-01069-1.
[13] Bai K, Yu X, Wen G, Yang Y, Lin Y, Zhang L, Rong J, Yin L-Ch, Qi W, Bonn M, Wang HI, Liu G. Spontaneous dissociation of excitons in polymeric photocatalysts for overall water splitting. Nat Commun 2025;16:8577. https://doi.org/10.1038/s41467-025-63590-0.
[14] Lin J, Hu K, Wang Y, Tian W, Hall T, Duan X, Sun H, Zhang H, Cortés E, Wang Sh. Tandem microplastic degradation and hydrogen production by hierarchical carbon nitride-supported single-atom iron catalysts. Nat Commun 2024;15:8769. https://doi.org/10.1038/s41467-024-53055-1.

[15] Wang X, Liu B, Ma S, Zhang Y, Wang L, Zhu G, Huang W, Wang S. Induced dipole moments in amorphous ZnCdS facilitate charge separation for efficient photocatalytic H_2 evolution. Nat Commun 2024;15:2600. https://doi.org/10.1038/s41467-024-47022-z.
[16] Luo H, Liu Zh, Lv H, Vequizo J Jhon M, Zheng M, Han F, Ye Zh, Yamakata A, Shangguan W, Lee AF, Wu X, Kazunari D, Lu J, Jiang Zh. Efficient and stable n-type sulfide for unassisted photocatalytic overall water splitting. Nat Commun 2025;16:8786. https://doi.org/10.1038/s41467-025-63840-1.
[17] Wu Q, Zhang X, Chen Y, Liu J, Li J, Lin H, Li Y, Li S, Zong X. Water-stable high-entropy metal-organic framework promoting charge separation for efficient photocatalytic hydrogen evolution. Adv Mater 2024;36:2403328. https://doi.org/10.1002/adma.202403328.
[18] Jin L, Li J, Li W, Wang H, Li Y, Wang Y, Wang X, Li J, Xiang Z, Jiang H. Arrangement of ordered donor-acceptor components in a metal-organic framework for cocatalyst-free photocatalytic hydrogen evolution with efficient proton conduction. Angew Chem Int Ed 2025;64:e202501141. https://doi.org/10.1002/anie.202501141.
[19] Xin X, Li Y, Zhang Y, Wang Y, Chi X, Wei Y, Diao C, Su J, Wang R, Guo P, Yu J, Zhang J, Sobrido AJ, Titirici M-M, Li X. Large electronegativity differences between adjacent atomic sites activate and stabilize $ZnIn_2S_4$ for efficient photocatalytic overall water splitting. Nat Commun 2024;15:337. https://www.nature.com/articles/s41467-024-44725-1.
[20] Yuan C, Yin H, Li J, Zhang Y, Chen H, Xiao D, Wang Q, Zhang Y. Light-induced CoO_x surface reconstruction in hollow heterostructure for durable photocatalytic seawater splitting. Nat Commun 2025;16:1–14. https://doi.org/10.1038/s41467-025-62033-0.
[21] Zhang Q, Zhang J, Zhang L, Yang F, Li L, Dai W-L. Black phosphorus quantum dots facilitate carrier separation for enhancing hydrogen production over hierarchical $Cu_7S_4/ZnIn_2S_4$ composites. Catal Sci Technol 2020;10:1030–9. https://doi.org/10.1039/C9CY02278C.
[22] Ma Q-L, Wei J, Lin Z, Guo Y, Tian H, Liu Q, Lin H, Su P, Tang Y. Enhanced photocatalytic performance of Ce^{3+}-doped $ZnIn_2S_4$ through vacancy engineering for efficient hydrogen evolution and pollutant degradation. Appl Catal B Environ Energy 2025;378:125547. https://doi.org/10.1016/j.apcatb.2025.125547.
[23] Gao F, Cui W-G, Wang X, Li Z, Chen Y, Shen Z, Wang K, Gao Y, Miao J, Yang Y, Chen J, Shen S, Pan H. Harnessing hydrogen spillover by lattice strain for enhanced photocatalytic hydrogen evolution of $ZnIn_2S_4$. ACS Catal 2025;15:2367–79. https://doi.org/10.1021/acscatal.4c07308.
[24] Zhang J, Hu L, Wu E, Yu B, Wang Q, Zhou W, Chen X, Bai J, Sun S. CuNiFe alloy-modified MWCNTs derived from waste battery leachate for enhanced photocatalytic H_2 evolution over $ZnIn_2S_4$. Adv Funct Mater 2025;35:2504286. https://doi.org/10.1002/adfm.202504286.
[25] Xiao X, Li S, Zuo L, Li R, Li Z, Liu L, Fan H, Li B. Twin S-scheme heterojunction $ZnO/UiO\text{-}66\text{-}NH_2@ZnIn_2S_4$ rhombic octahedra for efficient photocatalytic H_2 evolution. Adv Funct Mater 2025;35:2418778. https://doi.org/10.1002/adfm.202418778.
[26] Liu S, Zhang Y, Wang Y, Zhang X, Li Y, Wang H, Li J, Xiang Z, Jiang H. In-situ formation of spatially oriented interfacial Cu^0 in dual-plasmon resonance coupling $ZnIn_2S_4/Cu\text{-}Cu_{3-x}P$ heterojunction for full-spectrum photocatalytic hydrogen evolution. Adv Funct Mater 2026:e75215. https://doi.org/10.1002/adfm.75215.
[27] Li N, Zhang J, Ma J, Xue C, Chang Q, Liu L, Tian W. Efficient photocatalytic hydrogen evolution enabled by defect- and interface-induced dual built-in electric fields in a $ZnIn_2S_4$/1T–2H WS_2 heterojunction. Small 2026:e14954. https://doi.org/10.1002/smll.202514954.
[28] Lei H, Zhang J, Wu Z, Hong M. In-situ growth of $ZnIn_2S_4$ nanosheets on a Ti-based MOF to form a core-shell heterojunction for enhanced photocatalytic hydrogen evolution. Sci China Mater 2026. https://doi.org/10.1007/s40843-025-3875-1.
[29] Ahmad M, Wu K, Ahmed A, Adnan M, Rafiq M, Cong H, Yu B. Design and architecture of $ZnIn_2S_4$ and $ZnIn_2S_4$-based hybrid materials for photocatalytic, electrocatalytic and photoelectrochemical hydrogen evolution. J Mater Chem A 2025;13:6223–73. https://doi.org/10.1039/D4TA08155B.
[30] Wang J, Wei Y, Zhang B, Yang K, Huang W, Lu K. Recent progress on $ZnIn_2S_4$-based composite photocatalysts for photocatalytic hydrogen production coupling organic synthesis. J Mater Chem A 2025;13:39488. https://doi.org/10.1039/D5TA06861D.
[31] Lin J, Wang Y, Chen Y, Zhang X, Li Y, Wang H, Li J, Xiang Z, Jiang H. $ZnIn_2S_4$-based S-scheme heterojunction photocatalysts for efficient solar-to-chemical energy conversion. Coord Chem Rev 2026;553:217347. https://doi.org/10.1016/j.ccr.2026.217347.
[32] Xiong X, Chen Z, Liu S, Zhang Y. A dual-functional S-scheme Ti_3C_2/MoS_2- $ZnIn_2S_4$ heterojunction for accelerated photocatalytic H_2 evolution and efficient solar evaporators. J Mater Chem A 2025;13. https://doi.org/10.1039/D5TA00933B.
[33] Fan J, Song C, Zhang Y, Wang H, Zou J. Engineering MXenes charge bridge enables fast carrier transport in S-scheme heterojunctions for enhanced photocatalytic H_2 production. Appl Catal B Environ Energy 2026;385:126268. https://doi.org/10.1016/j.apcatb.2025.126268.
[34] Xu L, Iqbal R, Wang Y, Taimoor S, Hao L, Dong R, Liu K, Texter J, Sun Z. Emerging two-dimensional materials: synthesis, physical properties, and application for catalysis in energy conversion and storage. Innov Mater 2024;2:100060. https://doi.org/10.59717/j.xinn-mater.2024.100060.
[35] Zhu H, Liu Y, Wu Y, He Y, Cai Y, Zhu S. Electrocatalytic stability of two-dimensional materials. J Energy Chem 2024;97:302–20. https://doi.org/10.1016/j.jechem.2024.05.044.
[36] Ashraf T, Ali B, Ashraf S, Imran M, Tahir Fazal M, Iqbal J. Recent advancement in MXene based heterojunctions toward CO_2 photo-reduction and H_2 production applications: a review. FlatChem 2024;44:100620. https://doi.org/10.1016/j.flatc.2024.100620.
[37] Das P, Biswala L, Parida K. A review on MXene modified quantum dot photocatalysts for sustainable energy generation and environmental remediation. Catal Sci Technol 2025;23:6976–7003. https://doi.org/10.1039/D5CY00606F.
[38] Tayyab M, Kulsoom UE, Liu Y, Mansoor S, Khan M, Akmal Z, Mushtaq A, Arif M, Shamriaz U, Zhou L, Lei J, Zhang J. Visible light-driven photocatalytic H_2 evolution and dye degradation by electrostatic self-assembly of CdS nanowires on Nb_2C MXene. Int J Hydrogen Energy 2024;51:1400–13. https://doi.org/10.1016/j.ijhydene.2023.09.199.
[39] Zhang Q, Fan R, Cheng W, Ji P, Sheng J, Liao Q, Lai H, Fu X, Zhang C, Li H. Synthesis of large-area MXenes with high yields through power-focused delamination utilizing vortex kinetic energy. Adv Sci 2022;9:2202748. https://doi.org/10.1002/advs.202202748.
[40] Zhang Q, Zhang Z, Zhao D, Wang L, Li H, Zhang F, Huo Y, Li H. Synergistic photocatalytic-photothermal contribution enhanced by recovered Ag^+ ions on MXene membrane for organic pollutant removal. Appl Catal B Environ 2023;320:122009. https://doi.org/10.1016/j.apcatb.2022.122009.
[41] Zhang Q, Gu H, Wang X, Li L, Zhang J, Zhang H, Li Y, Dai W. Robust hollow tubular $ZnIn_2S_4$ modified with embedded metal-organic-framework-layers: extraordinarily high photocatalytic hydrogen evolution activity under simulated and real sunlight irradiation. Appl Catal B Environ 2021;298:120632. https://doi.org/10.1016/j.apcatb.2021.120632.
[42] Zhang Q, Fan R, Cheng W, Ji P, Sheng J, Liao Q, Lai H, Fu X, Zhang C, Li H. Synthesis of large-area MXenes with high yields through power-focused delamination utilizing vortex kinetic energy. Adv Sci 2022;9:2202748. https://doi.org/10.1002/advs.202202748.
[43] Uwadiunor E, Johnson D, Hansen K, Djire A. Controlling the surface reactivity of hybrid Ti_3CN MXene via in-situ electrocatalysis. ChemCatChem 2022;14:e202200702. https://doi.org/10.1002/cctc.202200702.
[44] Xu Y, Wang F, Lei S, Wei Y, Zhao D, Gao Y, Ma X, Li S, Chang S, Wang M, Jing H. In situ grown two-dimensional TiO_2/Ti_3CN MXene heterojunction rich in Ti^{3+} species for highly efficient photoelectrocatalytic CO_2 reduction. Chem Eng J 2023;452:139392. https://doi.org/10.1016/j.cej.2022.139392.
[45] Wang J, Chen Y, Zhou W, Tian G, Xiao Y, Fu H, Fu H. Cubic quantum dot/hexagonal microsphere $ZnIn_2S_4$ heterophase junctions for exceptional visible-light-driven photocatalytic H_2 evolution. J Mater Chem A 2017;18:8451–60. https://doi.org/10.1039/C7TA01914A.
[46] Wang B, Ding Y, Deng Z, Li Z. Rational design of ternary $NiS/CQDs/ZnIn_2S_4$ nanocomposites as efficient noble-metal-free photocatalyst for hydrogen evolution under visible light. Chin J Catal 2019;40:335–42. https://doi.org/10.1016/S1872-2067(18)63159-6.
[47] Li Y, Wang L, Zhang F, Zhang W, Shao G, Zhang P. Detecting and quantifying wavelength-dependent electrons transfer in heterostructure catalyst via in situ irradiation XPS. Adv Sci 2023;10:2205020. https://doi.org/10.1002/advs.202205020.
[48] Wang L, Li Y, Ai Y, Fan EC, Zhang F, Zhang W, Shao G, Zhang P. Tracking heterogeneous interface charge reverse separation in $SrTiO_3/NiO/NiS$ nanofibers with in situ irradiation XPS. Adv Funct Mater 2023;33:2306466. https://doi.org/10.1002/adfm.202306466.
[49] Li Y, Zhang Y, Hou R, Ai Y, Cai M, Shi Z, Zhang P, Shao G. Revealing electron numbers-binding energy relationships in heterojunctions via in-situ irradiated XPS. Appl Catal B Environ Energy 2024;356:124223. https://doi.org/10.1016/j.apcatb.2024.124223.
[50] Deng X, Zhang J, Qi K, Liang G, Xu F, Yu J. Ultrafast electron transfer at the In_2O_3/Nb_2O_5 S-scheme interface for CO_2 photoreduction. Nat Commun 2024;15:4807. https://doi.org/10.1038/s41467-024-49004-7.
[51] Sun J, Liu H, Wang S, Zhang Y, Bie C, Zhang L. In situ irradiated XPS investigation on S-scheme $ZnIn_2S_4$@COF-5 photocatalyst for enhanced photocatalytic degradation of RhB. J Materiomics 2025;11:100975. https://doi.org/10.1016/j.jmat.2024.100975.
[52] Ding M, Xiao R, Zhao C, Bukhvalov D, Chen Z, Xu H, Tang H, Xu J, Yang X. Evidencing interfacial charge transfer in 2D CdS/2D MXene schottky heterojunctions toward high-efficiency photocatalytic hydrogen production. Sol RRL 2020;5:2000414. https://doi.org/10.1002/solr.202000414.
[53] Cao L, Yang C, Zhang B, Lv K, Li M, Deng K. Synergistic photocatalytic performance of cobalt tetra (2-hydroxymethyl-1,4-dithiin) porphyrazine loaded on zinc oxide nanoparticles. J Hazard Mater 2018;359:388–95. https://doi.org/10.1016/j.jhazmat.2018.07.074.
[54] Zhu C, Liu CA, Fu Y, Gao J, Huang H, Liu Y, Kang Z. Construction of CDs/CdS photocatalysts for stable and efficient hydrogen production in water and seawater. Appl Catal B Environ 2019;242:178–85. https://doi.org/10.1016/j.apcatb.2018.09.096.
[55] Tie L, Yang S, Yu C, Chen H, Liu Y, Dong S, Sun J, Sun J. In situ decoration of ZnS nanoparticles with Ti_3C_2 MXene nanosheets for efficient photocatalytic hydrogen evolution. J Colloid Interface Sci 2019;545:63–70. https://doi.org/10.1016/j.jcis.2019.03.014.
[56] Xi Q, Yue X, Feng J, Liu J, Zhang X, Zhang C, Wang Y, Wang Y, Lv Z, Li R, Fan C. Facile synthesis of 2D $Bi_4O_5Br_2$/2D thin layer-Ti_3C_2 for improved visible-light photocatalytic hydrogen evolution. J Solid State Chem 2020;289:121470. https://doi.org/10.1016/j.jssc.2020.121470.
[57] Li J-Y, Li Y-H, Zhang F, Tang Z-R, Xu Y-J. Visible-light-driven integrated organic synthesis and hydrogen evolution over 1D/2D $CdS\text{-}Ti_3C_2T_x$ MXene composites. Appl Catal B Environ 2020;269:118783. https://doi.org/10.1016/j.apcatb.2020.118783.

[58] Zhang H, Gu H, Wang X, Li L, Zhang J, Chang S, Dai W-L. Embedding indium nitride at the interface of indium-oxide/indium-zinc-sulfide heterostructure with enhanced interfacial charge transfer for high photocatalytic hydrogen evolution. J Colloid Interface Sci 2022;622:539–48. https://doi.org/10.1016/j.jcis.2022.04.118.

[59] Chang S, Gu H, Zhang H, Wang X, Li Q, Cui Y, Dai W-L. Facile construction of a robust CuS@$NaNbO_3$ nanorod composite: a unique p-n heterojunction structure with superior performance in photocatalytic hydrogen evolution. J Colloid Interface Sci 2023;644:304–14. https://doi.org/10.1016/j.jcis.2023.04.111.

[60] Zuo G, Wang Y, Teo WL, Xie A, Guo Y, Dai Y, Zhou W, Jana D, Xian Q, Dong W, Zhao Y. Ultrathin $ZnIn_2S_4$ nanosheets anchored on $Ti_3C_2T_X$ MXene for photocatalytic H_2 evolution. Angew Chem Int Ed 2020;59:11287–92. https://doi.org/10.1002/anie.202002136.

[61] Li Z, Huang W, Liu J, Lv K, Li Q. Embedding CdS@Au into ultrathin $Ti_{3x}C_2T_y$ to build dual schottky barriers for photocatalytic H_2 production. ACS Catal 2021;11:8510–20. https://doi.org/10.1021/acscatal.1c02018.

[62] Miao Z, Wang Q, Zhang Y, Meng L, Wang X. In situ construction of S-scheme AgBr/BiOBr heterojunction with surface oxygen vacancy for boosting photocatalytic CO_2 reduction with H_2O. Appl Catal B Environ 2022;301:120802. https://doi.org/10.1016/j.apcatb.2021.120802.